optica

Mapping the electron band structure by intraband high-harmonic generation in solids

A. A. Lanin,[1,2] **E. A. Stepanov,**[1,2] **A. B. Fedotov,**[1,2,3,4] **and A. M. Zheltikov**[1,2,3,4,*]

[1]*Physics Department, International Laser Center, M. V. Lomonosov Moscow State University, Moscow 119992, Russia*
[2]*Russian Quantum Center, Skolkovo, Moscow Region 143025, Russia*
[3]*Department of Physics and Astronomy, Texas A&M University, College Station, Texas 77843, USA*
[4]*Kazan Quantum Center, A.N. Tupolev Kazan National Research Technical University, Chetaev 18a, Kazan 420126, Russia*
*Corresponding author: zheltikov@physics.msu.ru

High-harmonic generation (HHG) has recently been extended to solids, enabling all-optical reconstruction of electron band structure. However, material absorption of above-the-bandgap interband harmonics used for this purpose in earlier work limits the applicability of this promising technique. Here, sub-100-fs mid-infrared pulses tunable within the range of wavelengths from 5.0 to 6.7 μm are used to study HHG in ZnSe. Below-the-bandgap high-order harmonics generated by such driver pulses fall within the transparency range of a solid material, thus removing absorption-related limitations on the depth of HHG. Such harmonics are shown to be ideally suited to probe the nonlinearities of electron bands, enabling an all-optical mapping of the electron band structure in bulk solids. © 2017 Optical Society of America

High-order harmonic generation (HHG) in atomic gases is one of the key phenomena in strong-field laser–matter interactions [1], playing a central role in optical physics and rapidly growing attosecond technologies [2]. When applied to solid materials [3–5], the approaches of strong-field physics are subject to natural limitations, related to absorption and much lower laser damage thresholds of solids. As a reward, such solid-state extensions promise breakthroughs toward petahertz solid-state optoelectronics [6–8], open avenues toward attosecond science on the platform of solid-state materials, and suggest new all-optical methods for crystallographic analysis [3].

Similar to canonical, weak-field, nonlinear optics of solids, which distinguishes intra and interband optical nonlinearities [9], strong-field nonlinear-optical effects in solid dielectrics, including HHG, can be driven by intra and interband ultrafast electron dynamics [10–17]. In a close analogy with HHG in gases [18], the relative significance of intra and interband mechanisms of HHG in solids is a function of the driver wavelength and the

harmonic order [11,14]. While the interband mechanism tends to dominate above-the-band-gap HHG and grows in prominence for shorter-wavelength laser drivers, the intraband electron dynamics are often important for below-the-band-gap harmonics and longer-wavelength drivers. In agreement with this tendency, HHG in ZnO driven by 3.76-μm pulses has been shown to be dominated by the interband mechanism [4,11,12], while HHG by an intense terahertz driver has been demonstrated to provide important insights into the intraband dynamics of electrons and holes [5,19].

The tendency outlined above is in no way exhaustive. As a prominent example, intraband above-the-gap harmonics in the extreme ultraviolet range have been recently shown [20] to offer a powerful tool to analyze energy dispersion in electron conduction bands. In experiments presented here, HHG in solids is studied using mid-IR driver pulses within the wavelength range of 5.0–6.7 μm. In this wavelength region, a large group of below-the-bandgap high-order harmonics distinctly reflects, as our experiments show, ultrafast dynamics of electron wave packets within the conduction and valence bands. We demonstrate in this paper that these harmonics directly relate to the nonlinearities of electron bands, providing an ideal tool for electron band structure analysis in bulk solids (Fig. 1). Moreover, we extend the earlier work to retrieve the energy dispersion profile for one of the electron conduction bands of ZnSe and to show that the result of this retrieval is fully consistent with the first-principle analysis of the electron band structure of ZnSe.

In the experiments, we use a frequency-tunable source of ultrashort mid-IR pulses [22,23], which consists of two sequential stages of nonlinear-optical down conversion (Fig. S1, Supplement 1), involving optical parametric amplification (OPA) in two cascaded beta barium borate (BBO) crystals, both pumped by the amplified Ti: sapphire laser output, followed by difference-frequency generation (DFG) in an $AgGaS_2$ (AGS) crystal. The central wavelength of the DFG output can be tuned from 2.85 to 13 μm by rotating the AGS crystal. The spectrum of DFG radiation is measured with the use of a pyroelectric or cooled HgCdTe detector connected with a lock-in amplifier and a homebuilt monochromator. Mid-IR pulses are characterized (Fig. S2, Supplement 1) using cross-correlation frequency-resolved optical gating (XFROG) based on four-wave mixing in a gas [24,25].
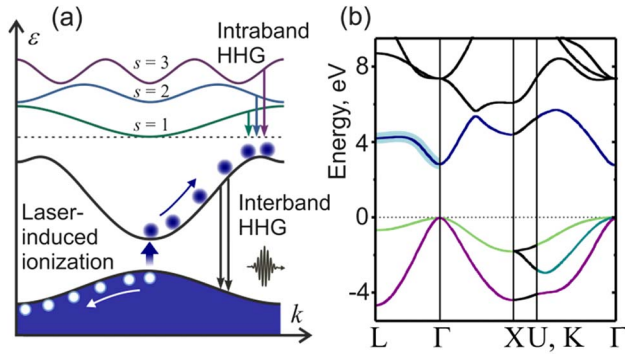
Fig. 1. (a) Inter and intraband HHG in a solid and electron band structure mapping. A laser driver field induces photoionization (vertical arrow), transferring electrons to the conduction bands, creating holes in the valence band, and driving the electron and hole wave-packet dynamics in the conduction and valence bands (shown by arrows). High-order harmonics are generated through the interband polarization involving electron–hole recombination (interband HHG), as well as through the modulation of the intraband current due to the nonlinearity of electron bands (intraband HHG). (b) The electron band structure of ZnSe as calculated in Ref. [21] (solid line), and the ΓL section of the conduction band reconstructed from the fit of HHG measurements (blue shading).

For HHG experiments, the two-stage OPA is adjusted to deliver signal and idler fields with central wavelengths tunable within the ranges of 1.41–1.46 μm and 1.87–1.96 μm, respectively. When mixed in the AGS crystal, these fields generate a mid-IR DFG output with a central wavelength λ_0 tunable from 5.0 to 6.7 μm, a pulse width of 85 fs, and an energy ranging from 7 μJ at $\lambda_0 \approx 5.0$ μm to 5 μJ at $\lambda_0 \approx 6.7$ μm. The mid-IR DFG output is separated from the signal and idler beams with a pair of CaF_2 wedge plates and is focused with a 20-cm-focal-length BaF_2 lens for additional, Fourier-plane spatial filtering with a 2-mm-diameter pinhole. A 15×, 0.30-NA reflective objective, placed at a distance of 40 cm from the lens, focused the mid-IR beam onto a 2-mm-thick ZnSe polycrystalline film with an average size of crystallites of about 50 μm. The beam-quality parameter for the focused mid-IR driver in this beam-focusing geometry was estimated by knife-edge measurements as $M^2 \approx 1.1$, delivering field intensities up to 4 TW/cm² at $\lambda_0 \approx 5.0$ μm and up to 2.6 TW/cm² at $\lambda_0 \approx 6.7$ μm in a focused mid-IR driver. With the refractive index of ZnSe at $\lambda \approx 5$ μm being $n \approx 2.4$, this translates into electric fields up to $E \approx 0.32$ V/Å at $\lambda_0 \approx 5.0$ μm and 0.26 V/Å at $\lambda_0 \approx 6.7$ μm inside the solid dielectric.

The mid-IR beam transmitted through the ZnSe film and optical harmonics generated in this sample were collimated with a 3.0-cm-focal-length CaF_2 lens and analyzed, following appropriate spectral separation, with a detection system based on three spectrometers intended for different frequency ranges (Fig. S1, Supplement 1). The spectra of the mid-IR driver and its second harmonic were measured using a homebuilt spectrometer consisting of a monochromator with replaceable 75-, 150-, and 300-grooves/mm gratings, a thermoelectrically cooled photoconductive HgCdTe detector, and a lock-in amplifier. The spectra of the second to seventh harmonics, reflected off a flip mirror (Fig. S1, Supplement 1), were measured using an infrared spectrometer for the 900–2500-nm wavelength range connected to a thermoelectrically cooled InGaAs linear image sensor. Finally, the spectra of higher order harmonics were analyzed with a standard Ocean Optics spectrometer for the visible and near-IR range.
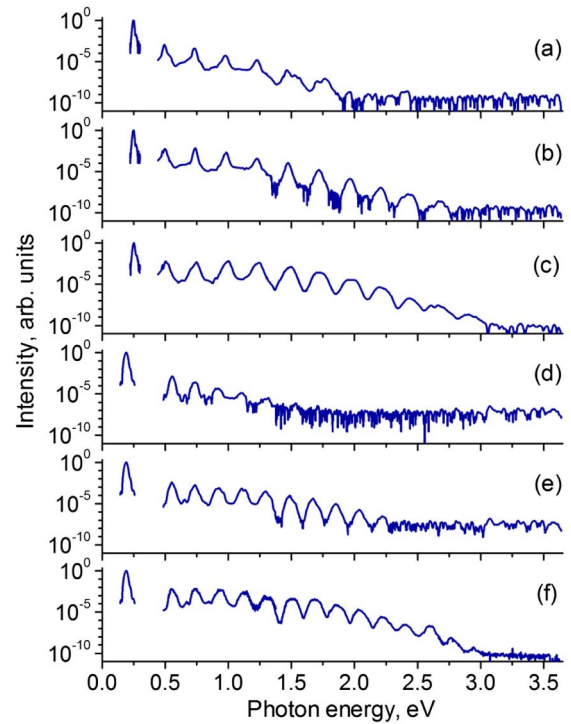
Fig. 2. Spectra of optical harmonics from a 2-mm-thick ZnSe film measured with a 85-fs mid-infrared driver with a central wavelength of 5.0 μm (a)–(c) and 6.7 μm (d)–(f). The driver intensity is 0.04 TW/cm² (a), 0.17 TW/cm² (b), 0.32 TW/cm² (c), 0.04 TW/cm² (d), 0.13 TW/cm² (e), and 0.19 TW/cm² (f).

The results of our HHG experiments are presented in Figs. 2 and 3. In the regime of low field intensities, $I_0 < 0.04$ TW/cm², the driver field inside the dielectric, $E_0 < 0.03$ V/Å, can only give rise to small corrections to the optical polarization. The spectra of optical harmonics generated in ZnSe in this regime feature a limited number of low-order optical harmonics [Figs. 2(a) and 2(d)], whose intensity rapidly decreases with the harmonic number. Both even and order harmonics are observed in these experiments as the lattice of zinc-blende ZnSe is optically isotropic, but noncentrosymmetric. When studied as functions of the driver intensity I_0 (Fig. 3), the intensities of individual optical harmonics in this low-intensity regime were found to follow the I_0^N scaling (dash–dotted lines in Fig. 3) with N being the harmonic number, indicating a canonical perturbative scenario of harmonic generation. For $I_0 < 0.10$ TW/cm², the high-N harmonic signal is below the noise level [Figs. 2(a) and 2(d)].

For field intensities $I_0 > 0.10$–0.15 TW/cm², the physics behind harmonic generation in a solid, as indicated by harmonic spectra measured in our experiments (Fig. 2), are drastically different. In this range of driver intensities, the harmonic spectra display well-resolved plateaus, followed by a cutoff [Figs. 2(b), 2(c), 2(e), and 2(f)]. As functions of the driver intensity, harmonic intensities in this regime considerably deviate from the I_0^N perturbative scaling, indicating a strongly nonperturbative regime of light–matter interactions (Fig. 3). For $I_0 > 0.2$–0.3 TW/cm², the harmonic spectra stretch as far as the edge of the band gap of ZnSe ($\Delta_0 \approx 2.8$ eV), continuing to extend further, beyond the band-gap edge, for higher I_0.

In a semiclassical picture of intraband HHG in solids [10,19], the momentum of an electron wave packet driven by the field
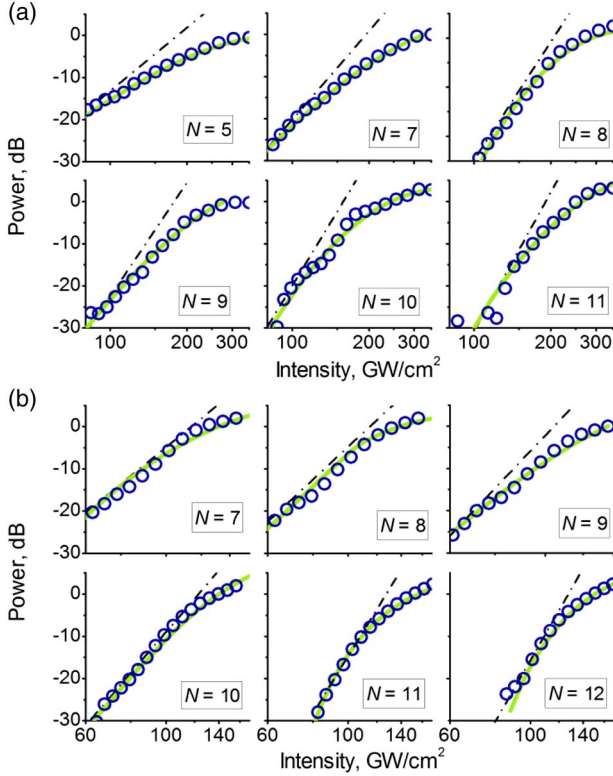
Fig. 3. Power of the Nth-order optical harmonic generated by a 85-fs driver pulse with a central wavelength of 5.0 μm (a) and 6.7 μm (b) in a 2-mm-thick ZnSe film as a function of the driver intensity I_0 for harmonic numbers N from 4 to 11 (a) and 5 to 12 (b), as shown in the panels. The dash–dotted lines show the I_0^N dependence. The solid lines presents the best fit of the experimental data with harmonic intensities calculated through the Fourier transform of dv/dt.

$E(t)$ is calculated by integrating the Bloch acceleration theorem [10,26], $k(t) = -(e/\hbar) \int_{-\infty}^t E(\theta) d\theta$, where e is the electron charge. For a driver intensity $I_0 \approx 0.3$ TW/cm², which translates into a driving field $E_0 \approx 0.1$ V/Å inside ZnSe, the momentum $k_e = eE_0/\hbar\omega_0$, which the electron picks up from the driver of frequency ω_0 as a part of its field-induced quiver motion, is estimated as $k_e \approx 0.22$ a.u. and 0.28 a.u. for $\lambda_0 = 5.0$ μm and 6.7 μm, respectively. Comparing these k_e values to the sizes of the zinc-blende ZnSe Brillouin zone along the most relevant, ΓL, ΓX, and ΓK axes of high symmetry (≈ 0.25 a.u., 0.29 a.u., and 0.31 a.u., respectively), we see that a field-induced electron quiver motion with such a momentum can probe the entire Brillouin zone, even reaching the Brillouin-zone edges when driven along the ΓL and ΓX directions. Optical harmonics generated by such electrons as a part of their dynamics (Fig. 1) will thus feature the signatures of electron band topology, enabling quantitative analysis of electron band anharmonicity.

The electron band structure is modeled by fitting the results of full band-structure analysis of ZnSe [21] [blue solid line in Fig. 1(b)] with a sum of five harmonic terms, $\varepsilon(k) = \varepsilon_0 + \sum_{s=1}^5 \varepsilon_s \cos(ska)$. The high-harmonic spectra are then calculated [19] by taking the Fourier transform of the time derivative of the intraband current, $j(t) = en_e v(t)$, where $v(t) = \hbar^{-1}(d\varepsilon/dk)|_{k(t)}$ is the velocity of the electron wave packet, n_e is the electron density in a given electron band, and $k(t)$ is found by integrating the Bloch acceleration theorem with $v(0) = 0$, that is, with electrons

and holes being at the Γ point at $t = 0$. The driver field is defined as $E(t) = E_0 \exp(-2 \ln 2\, t^2/\tau_0^2) \times [\cos \omega_0 t + \alpha \cos(2\omega_0 t + \phi_0)]$, where $\omega_0 = 2\pi c/\lambda_0$ and τ_0 is the FWHM pulse width. In calculations, we set $\tau_0 = 85$ fs. The $2\omega_0$ component is included to account for second-harmonic generation by the surface sources of quadratic nonlinearity, as well as by noncentrosymmetric polarization and currents in the bulk of ZnSe. The behavior of I_N as a function of I_0 for each N is insensitive to φ_0 and α, having no effect on our procedure of electron band structure reconstruction. In our calculations, we set $\varphi_0 = 0$ and take $\alpha = 0.02$ as a correct measure of second-harmonic generation efficiency.

The spectra of optical harmonics generated by the electron and hole wave packets moving along the respective conduction and valence bands (Fig. 1) of ZnSe in the field of a laser driver with $E_0 = 0.07$ V/Å, $\tau_0 = 85$ fs, and $\lambda_0 = 6.7$ μm are presented in Figs. S3a–S3d, Supplement 1. Since the nonlinearity of the electron conduction bands of ZnSe is strongest along the ΓL and ΓK symmetry axes of the ZnSe Brillouin zone, the electron wave packets driven along these directions emit the broadest harmonic spectra (purple and navy lines in Fig. S3d, Supplement 1), dominating the highest orders in HHG. The stronger nonlinearity of electron conduction band along the ΓL and ΓK axes helps isolate their contribution to HHG, even in experiments with polycrystalline samples, despite inevitable averaging over the orientation of single crystals within the focal volume. In an earlier work [20], a similar approach has been successfully implemented in experiments with polycrystalline SiO₂ films. Of these two directions, the ΓK axis provides a longer plateau (navy line in Fig. S3, Supplement 1), but the ΓL direction yields stronger harmonics below the band gap (purple line in Fig. S3, Supplement 1), allowing the $\varepsilon(k)$ profile to be retrieved from HHG measurements.

With the conduction and valence band structure of ZnSe included in the model through the $\varepsilon(k)$ profiles, as calculated in Ref. [21], the behavior of harmonic intensities I_N measured as functions of the laser driver intensity I_0 (circles in Fig. 3) agrees well with the predictions of our HHG model (solid lines in Fig. 3). For low I_0 ($I_0 < 0.04$ TW/cm², Fig. 3), the signature I_0^N perturbative-regime scaling was observed for harmonic intensities. The nonperturbative regime of HHG, when the $I_N(I_0)$ dependence no longer scales as I_0^N (Fig. 3) is of special interest here, as it enables the key parameters of the electron band structure to be retrieved from HHG spectra.

The amplitudes ε_s in the Fourier-series expansion of the $\varepsilon(k)$ landscape are determined by fitting the predictions of the intraband HHG model (solid lines in Figs. 3 and S4) to the experimental dependences of harmonic intensities I_N measured as functions of the laser driver intensity I_0 (circles in Figs. 3 and S4). As a part of this procedure (Supplement 1), the model predictions are simultaneously fit first to the six experimental $I_N(I_0)$ dependences measured with $\lambda_0 = 5.0$ μm [Fig 3(a)], that is, for $N = 5$, 7, 8, 9, 10, and 11, and then to six experimental $I_N(I_0)$ dependences measured with $\lambda_0 = 6.7$ μm [Fig. 3(b)], that is, $N = 7$, 8, 9, 10, 11, and 12, yielding two sets of five ε_s parameters, each providing the best fit for six experimental $I_N(I_0)$ dependences measured for two driver wavelengths. This fitting procedure yields ε_s amplitudes as specified in Table 1. These two sets of ε_s values are in perfect agreement with each other, and they agree very well with the amplitudes of Fourier harmonics of the $\varepsilon(k)$ profile found by a full band-structure analysis of ZnSe [21] for the ΓL section of the conduction band (see Table 1). The ΓL section

Table 1. Amplitudes of Fourier Harmonics ε_s of the $\varepsilon(k)$ Profile Found by a Full Band-Structure Analysis and Amplitudes ε_s as Retrieved from the Fit of HHG Measurements

s	ε_s from Full Band-Structure Analysis, a.u.	ε_s Retrieved from the Fit, a.u.	
		$\lambda_0 = 5.0\ \mu m$	$\lambda_0 = 6.7\ \mu m$
1	−0.0207	−0.018 ± 0.008	−0.017 ± 0.011
2	−0.0131	−0.016 ± 0.007	−0.012 ± 0.008
3	−0.0041	−0.004 ± 0.001	−0.003 ± 0.001
4	−0.0012	−0.001 ± 0.0002	−0.0014 ± 0.0003
5	−3.5 × 10⁻⁴	(−3 ± 2) × 10⁻⁴	(−3 ± 2) × 10⁻⁴

of the conduction band reconstructed with this procedure is shown by blue shading in Fig. 1(b).

Although the ε_s coefficients are treated as fitting parameters when theoretical predictions are compared with the experimental $I_N(I_0)$ dependences, the resulting ε_s values are then compared with the ε_s coefficients found as the amplitudes of Fourier harmonics of the dispersion $\varepsilon(k)$, calculated for ZnSe from the first principles [21]. The one-to-one map between $\varepsilon(k)$ and $I_N(I_0)$ dictated by our model of intraband HHG leaves no freedom to tweak any of the ε_s parameters, as they have to be compared with ε_s coefficients uniquely defined by $\varepsilon(k)$. That the ε_s values found by fitting experimental $I_N(I_0)$ dependences agree so remarkably well with the ε_s coefficients found through the Fourier-series expansion of an independently calculated $\varepsilon(k)$ dispersion suggests that intraband electron wave-packet dynamics plays a dominant role in the studied regime of HHG.

That individual high-order harmonics are observed as prominent well-resolved signals in HHG spectra from ZnSe for driver wavelengths as long as 6.7 µm is remarkable in its own right. This finding suggests that a sufficiently large fraction of electrons avoids considerable momentum change as a result of ultrafast scattering within the entire field cycle [4,19], providing a probe for electron band-structure analysis.

In a simplified case of a biharmonic driver field, $\tau_0 \to \infty$, with $\varphi_0 = 0$ and $\alpha/2(s\omega_B/\omega_0) \ll 1$, the intensities of harmonics induced by the intraband currents are given by $I_N \propto (N\omega_0)^2|\sum_{s=1} s\varepsilon_s a J_N(s\omega_B/\omega_0)|^2$ for odd N and $I_N \propto (N\omega_0)^2|\sum_{s=1}(2\omega_0)^{-1}s\varepsilon_s a\alpha s\omega_B(J_{N-2}(s\omega_B/\omega_0) + J_{N+2}(s\omega_B/\omega_0))|^2$ for even N, with $\omega_B = eE_0 a/\hbar$ being the Bloch frequency. When an electron band profile $\varepsilon(k)$ can be accurately fit with a few low-order Fourier harmonics, as in the case studied here, the map between $\varepsilon(k)$ and harmonic spectra may become especially simple (Fig. S4, Supplement 1). As a typical example, with ZnSe driven by a laser field with $E_0 = 0.07$ V/Å, $\tau_0 = 85$ fs, and $\lambda_0 = 5.0$ µm, harmonics with N ranging from 3 to 15 are generated, as calculations show, predominantly by conduction-band electron wave packets driven in the directions close to the ΓL axis. Moreover, generation of each of the $N = 5$, 7, and 9 harmonics is dominated in this regime by a single Fourier harmonic of the $\varepsilon(k)$ profile of this band, namely, $s = 3$ and 4. Similarly, with $E_0 = 0.07$ V/Å, $\tau_0 = 85$ fs, and $\lambda_0 = 6.7$ µm, the Fourier harmonics with $s = 3$ and 4 are mapped onto optical harmonics with $N = 7$, 9, and 11.

To summarize, below-the-bandgap high-order harmonics generated in zinc-blende ZnSe by ultrashort mid-infrared pulses tunable within the range of wavelengths from 5.0 to 6.7 µm are shown to be ideally suited to probe the nonlinearities of electron bands, enabling an all-optical mapping of the electron band structure. Intraband optical harmonics, generated below the band gap, fall within the transparency range of a solid material, thus removing absorption-related limitations on the depth at which optical harmonics are generated, facilitating HHG-based *in situ* electron band structure analysis in the bulk of solid materials.

See Supplement 1 for supporting content.

REFERENCES

1. T. Brabec and F. Krausz, Rev. Mod. Phys. **72**, 545 (2000).
2. P. B. Corkum and F. Krausz, Nat. Phys. **3**, 381 (2007).
3. S. Ghimire, A. D. DiChiara, E. Sistrunk, P. Agostini, L. F. DiMauro, and D. A. Reis, Nat. Phys. **7**, 138 (2010).
4. G. Vampa, T. J. Hammong, N. Thiré, B. E. Schmidt, F. Légaré, C. R. McDonald, T. Brabec, and P. B. Corkum, Nature **522**, 462 (2015).
5. M. Hohenleutner, F. Langer, O. Schubert, M. Knorr, U. Huttner, S. W. Koch, M. Kira, and R. Huber, Nature **523**, 572 (2015).
6. A. Schiffrin, T. Paasch-Colberg, N. Karpowicz, V. Apalkov, D. Gerster, S. Mühlbrandt, M. Korbman, J. Reichert, M. Schultze, S. Holzner, J. V. Barth, R. Kienberger, R. Ernstorfer, V. S. Yakovlev, M. I. Stockman, and F. Krausz, Nature **493**, 70 (2012).
7. M. Schultze, E. M. Bothschafter, A. Sommer, S. Holzner, W. Schweinberger, M. Fiess, M. Hofstetter, R. Kienberger, V. Apalkov, V. S. Yakovlev, M. I. Stockman, and F. Krausz, Nature **493**, 75 (2012).
8. F. Krausz and M. I. Stockman, Nat. Photonics **8**, 205 (2014).
9. P. N. Butcher and D. Cotter, *The Elements of Nonlinear Optics* (Cambridge University, 1990).
10. D. Golde, T. Meier, and S. W. Koch, Phys. Rev. B **77**, 075330 (2008).
11. G. Vampa, C. R. McDonald, G. Orlando, D. D. Klug, P. B. Corkum, and T. Brabec, Phys. Rev. Lett. **113**, 073901 (2014).
12. G. Vampa, T. J. Hammond, N. Thiré, B. E. Schmidt, F. Légaré, C. R. McDonald, T. Brabec, D. D. Klug, and P. B. Corkum, Phys. Rev. Lett. **115**, 193603 (2015).
13. T. Higuchi, M. I. Stockman, and P. Hommelhoff, Phys. Rev. Lett. **113**, 213901 (2014).
14. G. Vampa, C. R. McDonald, G. Orlando, P. B. Corkum, and T. Brabec, Phys. Rev. B **91**, 064302 (2015).
15. P. G. Hawkins, M. Y. Ivanov, and V. S. Yakovlev, Phys. Rev. A **91**, 013405 (2015).
16. M. Wu, S. Ghimire, D. A. Reis, K. J. Schafer, and M. B. Gaarde, Phys. Rev. A **91**, 043839 (2015).
17. G. Ndabashimiye, S. Ghimire, M. Wu, D. A. Browne, K. J. Schafer, M. B. Gaarde, and D. A. Reis, Nature **534**, 520 (2016).
18. P. B. Corkum, Phys. Rev. Lett. **71**, 1994 (1993).
19. O. Schubert, M. Hohenleutner, F. Langer, B. Urbanek, C. Lange, U. Huttner, D. Golde, T. Meier, M. Kira, S. W. Koch, and R. Huber, Nat. Photonics **8**, 119 (2014).
20. T. T. Luu, M. Garg, S. Yu. Kruchinin, A. Moulet, M. T. Hassan, and E. Goulielmakis, Nature **521**, 498 (2015).
21. E. Ghahramani, D. J. Moss, and J. E. Sipe, Phys. Rev. B **43**, 9700 (1991).
22. A. A. Lanin, A. A. Voronin, E. A. Stepanov, A. B. Fedotov, and A. M. Zheltikov, Opt. Lett. **39**, 6430 (2014).
23. A. A. Lanin, A. A. Voronin, E. A. Stepanov, A. B. Fedotov, and A. M. Zheltikov, Opt. Lett. **40**, 974 (2015).
24. Y. Nomura, H. Shirai, K. Ishii, N. Tsurumachi, A. A. Voronin, A. M. Zheltikov, and T. Fuji, Opt. Express **20**, 24741 (2012).
25. A. A. Lanin, A. A. Voronin, A. B. Fedotov, and A. M. Zheltikov, Sci. Rep. **4**, 6670 (2014).
26. F. Bloch, Z. Phys. **52**, 555 (1929).